Frictional properties of natural fault gouge from a low-angle normal fault, Panamint Valley, California

T. Numelin,[1,2] C. Marone,[1] and E. Kirby[1]

Received 23 October 2005; revised 1 October 2006; accepted 20 November 2006; published 16 March 2007.

[1] We investigate the relationship between frictional strength and clay mineralogy of natural fault gouge from a low-angle normal fault in Panamint Valley, California. Gouge samples were collected from the fault zone at five locations along a north–south transect of the range-bounding fault system, spanning a variety of bedrock lithologies. Samples were powdered and sheared in the double-direct shear configuration at room temperature and humidity. The coefficient of friction, μ, was measured at a range of normal stresses from 5 to 150 MPa for all samples. Our results reinforce the intuitive understanding that natural fault gouge zones are inherently heterogeneous. Samples from a single location exhibit dramatic differences in behavior, yet all three were collected within a meter of the fault core. For most of the samples, friction varies from $\mu = 0.6$ to $\mu = 0.7$, consistent with Byerlee's law. However, samples with greater than 50 wt % total clay content were much weaker ($\mu = 0.2–0.4$). Expandable clay content of the samples ranged from 10 to 40 wt %. Frictional weakness did not correlate with expandable clays. Our results indicate that friction decreases with increasing total clay content, rather than with the abundance of expandable clays. The combination of field relations, analytical results, and friction measurements indicates a positive correlation between clay content, fabric intensity, and localization of strain in the fault core. A mechanism based upon foliations enveloping angular elements to reduce friction is suggested for weakening of fault gouge composed of mixed clay and granular material. We provide broad constraints of 1–5 km on the depth of gouge generation and the depth at which fault weakness initiates. We show that slip on the Panamint Valley fault and similar low-angle normal faults is mechanically feasible in the mid-upper crust if the strength of the fault is limited by weak, clay-rich fault gouge. **Citation:** Numelin, T., C. Marone, and E. Kirby (2007), Frictional properties of natural fault gouge from a low-angle normal fault, Panamint Valley, California, *Tectonics*, *26*, TC2004, doi:10.1029/2005TC001916.

[1]Department of Geosciences, Pennsylvania State University, University Park, Pennsylvania, USA.
[2]Now at ExxonMobil Exploration Company, Houston, Texas, USA.

0278-7407/07/2005TC001916

1. Introduction

[2] Since their recognition in the Basin and Range [*Longwell*, 1945], low-angle normal faults (LANFs) have been observed in extensional terranes worldwide [*Wernicke*, 1995]. Despite their widespread occurrence and the geologic evidence indicative of active slip on shallowly dipping planes [*Wernicke*, 1995; *Cichanski*, 2000; *Floyd et al.*, 2001; *Hayman et al.*, 2003; *Collettini and Holdsworth*, 2004; *Collettini et al.*, 2006], two robust arguments against slip on low-angle normal faults promulgate debate. The first is a purely mechanical argument, rooted in principles of Anderson-Byerlee fault mechanics [*Anderson*, 1951]. Anderson assumed that for an extending crust the principal stresses are orthogonal, with σ_1 oriented vertical to the free surface of the Earth. Assuming a coefficient of friction equal to 0.6, slip on normal faults is not favored when the angle between the normal to the fault plane and the maximum principle stress σ_1 is less than 30°. In the absence of unusual weakening mechanisms, Coulomb-Mohr failure criteria suggest that formation of new high-angle faults is favored over active slip on existing fault planes dipping less than 30° [*Handin*, 1969; *Scholz*, 2002]. The second argument contends that, despite rare examples of seismic slip on low-angle planes [*Caskey et al.*, 1996; *Abers et al.*, 1997; *Piccinini et al.*, 2003], the overall (global) lack of observed seismicity on low-angle faults provides strong empirical evidence against active slip [*Molnar and Chen*, 1982; *Jackson and White*, 1989; *Thatcher and Hill*, 1991].

[3] Several kinematic models have been proposed to reconcile the constraints Anderson's assumptions place on the orientation of active fault planes with observed LANF geometries. Perhaps the most well-known of these is the rolling hinge model [*Wernicke and Axen*, 1988], this model suggests that low-angle structures initiated at shallow dips in the lower crust, were active as high-angle normal faults while the footwall rebounded isostatically, and then rotated to low dip angles by subsequent uplift of the footwall. Active slip ceases as the fault planes are rotated to dips <30°. The rolling hinge model explains observed LANF geometries, but does not explain the phenomenon of active slip on shallowly dipping faults. Alternatively, *Yin* [1989] and *Westaway* [1999] considered the problem of how low-angle normal faults might initiate within intact rock. They proposed that to break new low-angle normal faults required that σ_1 must rotate at depth from the vertical orientation at the Earths free surface assumed by Anderson.

[4] A second class of explanations considers the micromechanics of the fault zone to explain slip on shallowly dipping faults. The range of favorable orientations for normal faulting described by Anderson do not consider

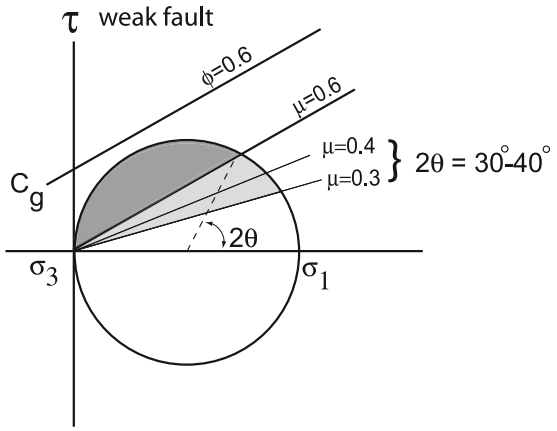

Figure 1. Mechanics of low-angle faulting. Mohr diagram describes low-friction weakening mechanism. Byerlee friction for most lithologies ($\mu = 0.6$) predicts that all faults oriented such that $2\Theta > 60°$ (dark shaded region) are unstable. However, some clay minerals have $\mu \ll 0.6$. Here the unstable region has been expanded (light shaded region) to include the shallowly dipping fault (15°–20°) that we observed in Panamint Valley, California. The orientation of this fault implies that it may be anomalously weak, e.g., $\mu \sim 0.3–0.4$.

the effect of an anomalously weak fault zone. Two of the most common explanations for weak fault zones are elevated pore pressures within the fault zone proper [*Axen*, 1992; *Rice*, 1992], and/or the presence of intrinsically weak fault gouge [*Hayman et al.*, 2003; *Axen*, 2004]. Mechanisms for both of these phenomena are geologically reasonable and relatively intuitive. Though examples of overpressure are uncommon in extensional settings, provided fluid pressure does not exceed $\sigma_3 + T$ (T = rock tensile strength), the shear stress supported by the fault zone is lower than the shear stress supported by the surrounding rocks, enabling fault reactivation at lower dip than predicted by Byerlee. In laboratory studies, synthetic fault gouge containing expandable clay minerals has been found to yield coefficient of friction (μ) values between 0.1 and 0.3, much lower than the $\mu = 0.6–0.8$ assumed from Byerlee's law (Figure 1) [*Scholz*, 2002].

[5] A number of recent claims employ kinematic evidence to demonstrate that normal faults are presently active at low dip angles [e.g., *Wernicke*, 1995; *Axen*, 1999; *Cichanski*, 2000; *Hayman et al.*, 2003]. These systems provide an opportunity to examine aspects of the mechanical controls (e.g., friction, pore pressure) on fault slip. In particular, for estimates of the coefficient of friction on faults μ_f, Byerlee values of 0.6 to 0.8 are often cited, regardless of the composition and texture of the fault rocks. Although conservative, $\mu_f \sim 0.6$ to 0.8 may not accurately reflect the frictional strength of the fault or fault gouge containing clay minerals [*Brown et al.*, 2003; *Hayman et al.*, 2003; *Saffer and Marone*, 2003]. Accurate estimation of the frictional strength of the fault gouge, μ_g, is important because questions remain as to how the mechanical (frictional) properties of the fault gouge may influence the overall mechanical strength of the fault, $\mu_f \propto \mu_g$.

[6] In this study, we exploit the spectacular preservation and exposure of gouge-mantled low-angle normal faults in Panamint Valley. The primary goal of our study is to characterize the frictional properties of natural fault gouge from the Panamint Valley Fault Zone, a well-known LANF [*Burchfiel et al.*, 1987; *MIT 1985 Field Geophysics Course and Biehler*, 1987] that formed at a low dip angle and appears to be actively deforming [*Kirby et al.*, 2003]. We evaluate the relationship between frictional strength, clay mineralogy, and gouge composition. Previous studies have shown that pure clay minerals such as montmorillonite are potentially very weak, with friction coefficients well below 0.6 [*Byerlee*, 1978; *Morrow et al.*, 1982, 2000; *Saffer et al.*, 2001; *Brown et al.*, 2003; *Saffer and Marone*, 2003]. We seek to test the hypothesis that fault weakness may be caused by naturally occurring abundances of clay minerals within fault gouge.

2. Tectonic Setting

[7] Panamint Valley is located in eastern California just east of the Slate Range (Figure 2). The physiographic valley is a type example of a pull-apart basin [*Burchfiel and*

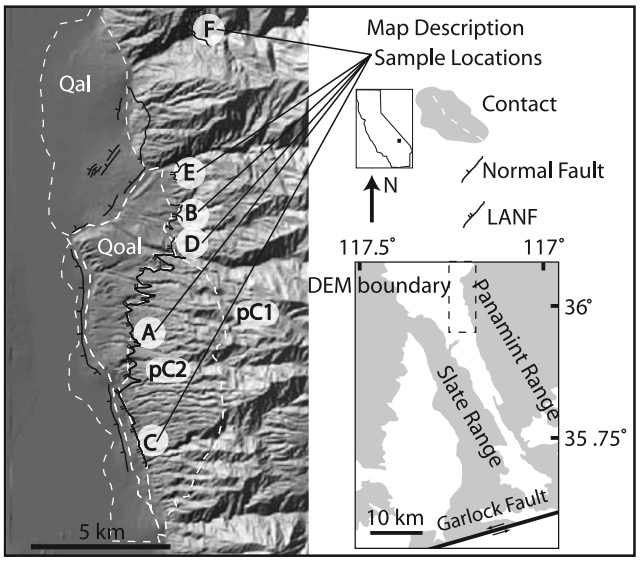

Figure 2. Central Panamint Valley, California. Study area extent is shown as the boxed region on the schematic illustration of Panamint and Slate Ranges. The shaded digital elevation model (DEM) was mosaiced from USGS 7.5 arc min DEM series. Two generations of alluvial fans are outlined, Quaternary alluvium (Qal), and older alluvium (Qoal), along with traces of minor alluvial faults [*Kirby et al.*, 2003]. The surface trace of the low-angle normal fault (LANF) is shown by the heavy black line, which separates alluvium from Paleozoic bedrock (pC1, pC2) of the exposed dip slope [*Andrew and Walker*, 2003]. Sample locations are annotated with arrows pointing to the location from which each gouge sample was extracted.

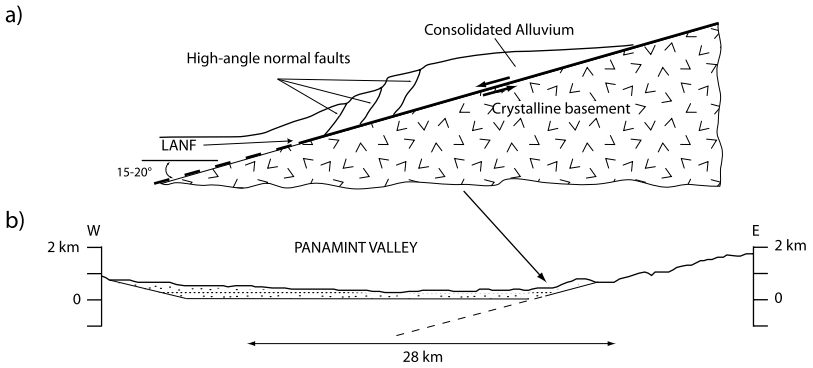

Figure 3. (a) Schematic (not to scale) cross section of the rooted low-angle normal fault, exposed in incised canyons on the eastern edge of Panamint Valley (Figure 3b). The dip varies along-strike between 15° and 20°. The hanging wall consists of consolidated Tertiary/Quaternary alluvium. Normal faults in the hanging wall dip ~60° and are thought to be kinematically linked to the low-angle fault at the contact between the alluvial deposits and the footwall [*Kirby et al.*, 2003]. The footwall is composed of pre-Cambrian gneisses, and is cut by the low-angle normal fault. Although heavily brecciated, we did not observe any steep throughgoing fractures in the footwall. (b) Scaled E–W cross section through central Panamint Valley.

Stewart, 1966], bound by the Panamint Valley/Hunter Mountain fault system on the east and north. The valley tapers from a width of ~28 km at its midpoint (Figures 2 and 3b) to less than 3 km at the southern end before intersecting the Garlock fault. Gravity surveys in northern Panamint Valley reveal that the sedimentary basin fill is less than 200 m thick [*MIT 1985 Field Geophysics Course and Biehler*, 1987] (Figure 3b).

[8] *Burchfiel et al.* [1987] argued that Panamint Valley and Saline Valley opened as twin pull-apart structures linked by the right-lateral Hunter Mountain fault. Palinspastic restoration of piercing points formed by the subvertical wall of the Hunter Mountain batholith with its country rock and a subhorizontal basalt flow (circa 4 Ma) across the fault indicate that Panamint Valley opened via oblique normal slip on a shallowly dipping (0°–15°) fault system [*Burchfiel et al.*, 1987]. Although the range-bounding fault in northern Panamint Valley appears to be Pliocene or younger, Miocene slip on a low-angle detachment is recorded in the northern Panamint range on the Emigrant fault [*Hodges et al.*, 1990], which apparently controlled subsidence and sediment accumulation in the Nova basin [*Snyder and Hodges*, 2000]. These two fault systems merge at the range front near Wildrose Canyon. South of this intersection, the modern range front fault system appears to have been active since Miocene time [*Andrew and Walker*, 2003]. Oblique-dextral slip on fault scarps that offset Pleistocene-recent alluvial fans indicate continued activity on this fault [*Smith*, 1973; *Zhang et al.*, 1990; *Kirby et al.*, 2003].

[9] In our study area (Figure 2), the low-angle normal fault is exposed in numerous canyons that have incised through older Pleistocene alluvial deposits into the underlying bedrock. The fault surface dips gently basinward 15°–20° and places poorly sorted, moderately indurated alluvial fan gravels atop heavily brecciated footwall rocks (Figure 3a). Footwall lithologies consist mostly of quartzofeldspathic gneisses, but in some locations, carbonates are present. Although the footwall is heavily brecciated along with the development of planar fabric elements, we

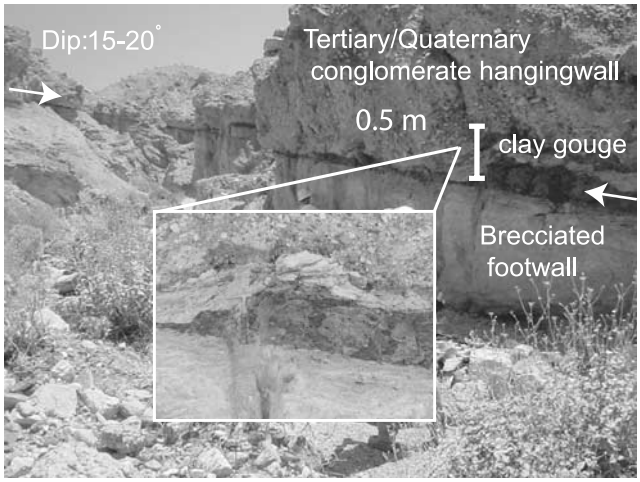

Figure 4. Photograph looking southeast at sample location A. The low-angle normal fault is clearly exposed in the sidewall of the gully. Arrows highlight fault dipping 15°–20° to the west. The footwall is composed primarily of exhumed Proterozoic gneisses and becomes progressively more brecciated closer to the fault core. The gouge zone is composed of fine-grained clay minerals and small quartzofeldspathic clasts derived from the footwall. Thickness varies from a few centimeters to almost 0.5 m as shown in this photograph. Virtually no material from the hanging wall is incorporated into the gouge zone. The hanging wall is made up of poorly to moderately indurated Tertiary debris flow deposits and alluvial gravels. Inset is a zoomed in photograph of fault core.

Figure 5. SEM images of disaggregated fault gouge used in friction experiments. Magnification is 100×. These three images represent the range in abundance of clay-sized grains among our sample suite. Note the abundance of fine, clay minerals in the image to the far left and the predominance of coarser clasts in the image to the far right.

observed that the intensity of the deformation (especially foliation) tends to decrease away from the fault core. A fine-grained, intensely foliated gouge zone approximately 0.1–1.0 m thick separates the hanging wall from the footwall (Figure 4). It is composed of clay-sized material with occasional clasts of footwall breccia. Incorporation of hanging wall clasts into the gouge zone is rare. The gouge zone is typically stratified into an intensely foliated fault core, surrounded by less foliated lithologies. Qualitatively, these regions of the fault zone exhibit slightly different colors and/or particle size distributions.

3. Methods

3.1. Field Observations and Sampling

[10] We chose six sampling sites (labeled A–F on Figure 2) along the central portion of the Panamint Range (Figure 2), based on the quality of the exposure and accessibility to the fault core. Qualitative examinations of the fault zone at each sampling site revealed that more than one distinct gouge composition was present. Typically, the observable clay content (as judged by relative "stickiness" of dry and wetted hand samples) and degree of fabric development increased closer to the fault core. These lithologies were stratified across the gouge zone from the intensely foliated fault core outward toward the footwall or hanging wall. We collected samples across the gouge zone at each sampling site and gave the distinct gouge lithologies numeric descriptors (e.g., A1, A2, A3). Natural fault gouge samples were collected by excavating a 20 cm × 20 cm × 20 cm cavity into the fault zone, from exposures in the sidewall of incised channels (Figure 4). After discarding the excavated material, we collected unweathered gouge for laboratory experiments. The sampling technique does not preserve any of the inherent fabric developed in the fault gouge, as our experimental methods are optimized for remoulded granular media (see below). The gouge samples were disaggregated using a jaw crusher until the resulting sample material matched the size distributions of the grains comprising the fault gouge. We assume this technique only disaggregated the clay-rich fault gouge and did not appreciably fracture grains. Disaggregated samples were passed through a 354 μm screen; all fractions smaller than 354 μm were retained for use in experiments. This technique ensures an equivalent particle size range for all samples; however, it should be noted that it does not necessarily produce a uniform particle size distribution (Figure 5). Disaggregated sample material was stored dry at room temperature and humidity.

3.2. Experimental Techniques

[11] Experimental gouge zones were constructed on the 5 cm × 5 cm side blocks of a double-direct shear sample assembly (Figure 6). We prepared layers with a uniform initial thickness of 7 mm using a precision leveling jig and surrounded the perimeter of the side blocks with a flexible adhesive membrane. Grooved surfaces of the forcing blocks ensured that shear occurred within the gouge layer, and not at the layer boundaries. Once the sample assembly was placed into the deformation rig, normal stress was applied and gouge layer compaction was measured. The initial thickness of the gouge layers was measured in situ to ±0.1 mm using digital calipers. This constraint on initial layer thickness was used for establishing a reference thickness from which we measured changes in layer thickness continuously during shear. Volumetric strain and shear strain were determined from these digital records. Layers were sheared at room temperature and humidity under nominally dry conditions. Samples were not baked prior to shearing. Under these conditions, adsorbed water and water expelled from the clay structure could potentially cause lubrication or excess pore pressure, which would simulate the quasi-undrained conditions expected in the core of clay-rich fault zones [e.g., *Vrolijk and van der Pluijm*, 1999].

[12] Our experiments were performed using a servo-hydraulic biaxial deformation rig, instrumented with direct current displacement transducers (DCDTs) to record displacement of the hydraulic rams, and Be-Cu strain gauge load cells to record applied force (Figure 6). These param-

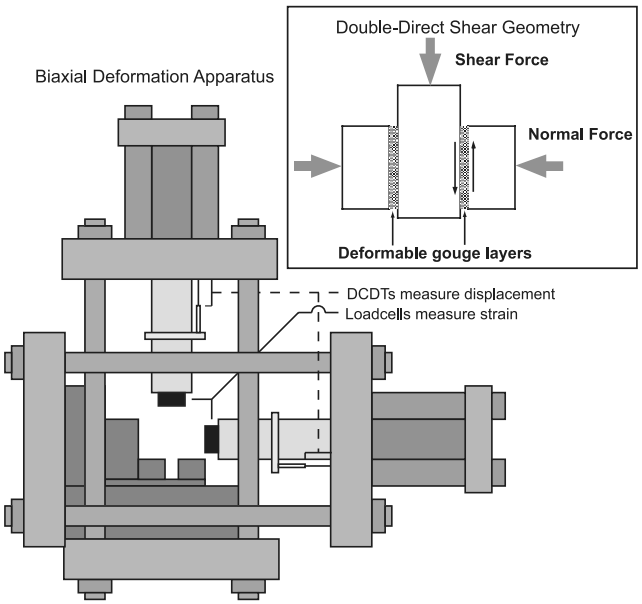

Figure 6. Schematic diagram of biaxial deformation apparatus. Inset shows double-direct shear forcing block assembly. The 7 mm thick gouge layers are sandwiched between grooved steel forcing blocks. Side blocks are 5 cm by 5 cm. Forcing block is 5 cm by 12 cm, resulting in a frictional contact area of 25 cm^2 during shear displacement. Experiments are carried out in displacement feedback via servo-control coupled to a vertically mounted direct current displacement transducer (DCDT). Compaction is measured via a horizontally mounted DCDT. Forces are measured by a pair of Be-Cu load cells, and stresses are calculated based on forcing block specifications.

eters are recorded continuously during each experiment. Vertical displacement was servo-controlled with displacement feedback via the DCDT mounted on the ram flange. Constant normal stress was maintained by servo-control with load feedback from the horizontal load cell.

[13] During each experiment, we ran computer-controlled displacement histories at different normal stresses, which were set by the operator during the experiment (Table 1). Time, load point displacement, and applied load were recorded continuously at 10 kHz. We filtered this to a sampling rate of 100 Hz and processed the data, calculating: friction, shear stress, normal stress, shear strain, and layer thickness (Figure 7).

[14] Our experiments were designed to investigate frictional strength and its variation with slip velocity for normal stresses ranging from 5 to 150 MPa, approximating the upper 5 km of the lithosphere. With the exception of the first normal stress in each experiment, we repeated the same displacement history at each normal stress. Because our remoulded samples do not retain any fabric from their in situ position, we conduct a "run-in" at the beginning of each experiment, to establish a steady state particle size distribution and fabric [*Marone*, 1998]. During initial compaction, grain contact area increases and strain hardening occurs until grains align and fabric evolves. At this point strain hardening ceases and a steady state coefficient of sliding friction is established (Figure 8) [*Saffer and Marone*, 2003]. Our initial load history consists of constant velocity load point displacement at 20 μm/s for 10 mm (Figure 8). In some of the high normal stress (100–150 MPa) experiments, load point displacement of 15 mm was required to achieve a steady state coefficient of friction.

[15] To evaluate the slip rate dependency of friction, we ran velocity stepping tests at each normal stress. Abrupt changes in load point velocity are imposed and the velocity dependence of sliding friction (μ) is reported as $(a-b) = \Delta\mu/\Delta\ln V$, where V is sliding velocity (Figure 9). Positive values of $a-b$ reflect velocity strengthening frictional behavior, leading to stable-sliding [*Marone*, 1998; *Scholz*, 2002]. Negative values of $(a-b)$ reflect velocity weakening which is a necessary condition for unstable stick-slip sliding [*Ruina*, 1983]. In our velocity stepping tests load point velocity alternates between 10 and 50 μm/s for displacement intervals of 500 μm.

[16] Although we do not report on effects of frictional healing tests in this paper, our experiments included slide-hold-slide tests to evaluate time- and slip-dependent frictional restrengthening [*Marone*, 1998]. These test cycles consisted of displacements of 200 μm at 20 μm/s followed by variable hold periods, increasing from 3 s to 1000 s.

3.3. Material Characterization

[17] Conventional powder X-ray diffraction was performed to characterize the bulk mineralogy of each gouge

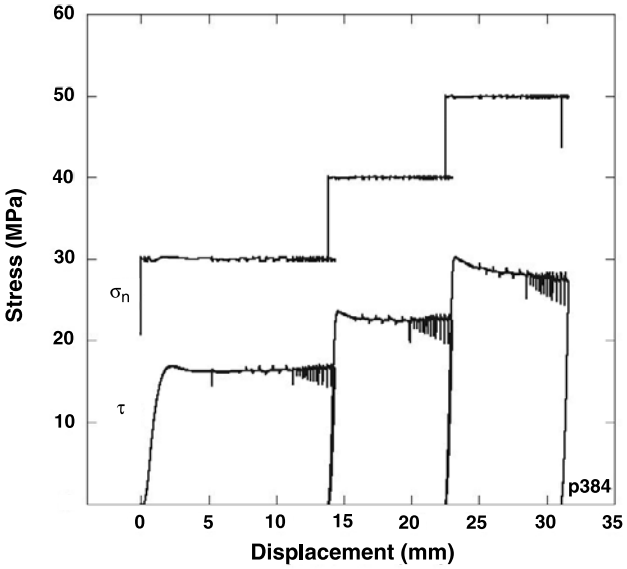

Figure 7. Experiments typically consisting of 3–4 normal stress steps, with loading histories as shown in Figure 8. Here we show both the normal stress and shear stress plotted against load point displacement for a typical experiment. Velocity stepping and slide-hold-slide tests run at each normal stress step reveal constitutive behavior of experimental faults. Slide-hold-slide tests allow examination of any time-dependent healing effects.

Table 1. Friction Experiments

Experiment	Sample	Location, UTM		Normal Stress, MPa
		Easting	Northing	
p383	A1	481899	3984056	5 10 15 20
p384	A1	481899	3984056	30 40 50
p402	A1	481899	3984056	70 80
p388	A1	481899	3984056	100 125 150
p390	A2	481899	3984056	5 10 15 20
p391	A2	481899	3984056	30 40 50
p403	A2	481899	3984056	70 80
p392	A2	481899	3984056	100 125 150
p228	A3	481899	3984056	5 10 15 20
p239	A3	481899	3984056	30 40 50
p370[a]	A3	481899	3984056	70 80
p310	A3	481899	3984056	100 125 150
p303	B4	483605	3988940	5 10 15 20
p307	B4	483605	3988940	30 40 50
p404	B4	483605	3988940	70 80
p309	B4	483605	3988940	100 125 150
p334	B5	483605	3988940	5 10 15 20
p327	B5	483605	3988940	30 40 50
p376	B5	483605	3988940	70 80
p328	B5	483605	3988940	100 125 150
p244	B6	483605	3988940	5 10 15 20
p273	B6	483605	3988940	30 40 50
p407[a]	B6	483605	3988940	70 80
p285	B6	483605	3988940	100 125 150
p270	C7	482449	3980325	5 10 15 20
p247	C7	482449	3980325	30 40 50
p382	C7	482449	3980325	70 80
p293	C7	482449	3980325	100 125 150
p344	D8	483295	3987673	5 10 15 20
p323	D8	483295	3987673	30 40 50
p408	D8	483295	3987673	70 80
p326	D8	483295	3987673	100 125 150
p345	E9	483952	3991127	5 10 15 20
p348	E9	483952	3991127	30 40 50
p381	E9	483952	3991127	70 80
p350	E9	483952	3991127	100 125 150
p356	F10	481967	3995187	5 10 15 20
p361	F10	481967	3995187	30 40 50
p394	F10	481967	3995187	70 80
p362	F10	481967	3995187	100 125 150

[a]Experiment failed.

sample. In addition, we prepared oriented clay separates to better characterize the clay mineral phases of each sample [*Moore and Reynolds*, 1997]. All interpretation was performed using TOPAS software from Bruker AXS®. TOPAS performs a Rietveld refinement on the diffraction pattern resulting in a modeled diffraction pattern that closely matches the original data [*Rietveld*, 1969]. These analytical procedures allowed us to relate the clay composition of gouge material to measured frictional properties.

4. Results

4.1. Gouge Composition and in Situ Context

[18] X-ray diffractograms reveal discernable peaks for chlorite, kaolinite, and muscovite, as well as a broad peak for undifferentiated swelling clays, composed of illite and smectite. Ethylene glycolation allows us to estimate the

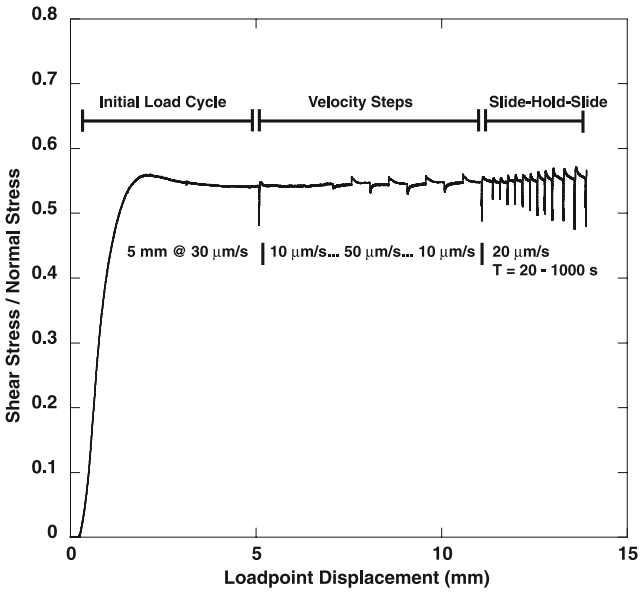

Figure 8. Normalized shear strength plotted against load point displacement at a single normal stress (30 MPa) during a typical experiment. The initial load cycle is run at a constant velocity to bring frictional response to quasi-steady state before the other load cycles are initiated. Velocity stepping tests and slide-hold-slide tests are run for each normal stress in all experiments. Velocity steps reveal stick-slip versus stable-sliding behavior, while slide-hold-slide tests reveal any postslip healing effects. Velocity steps alternate between 10 and 50 μm/s. Slide-hold-slide tests are performed at a single driving velocity and hold time, from 1 to 3000 s.

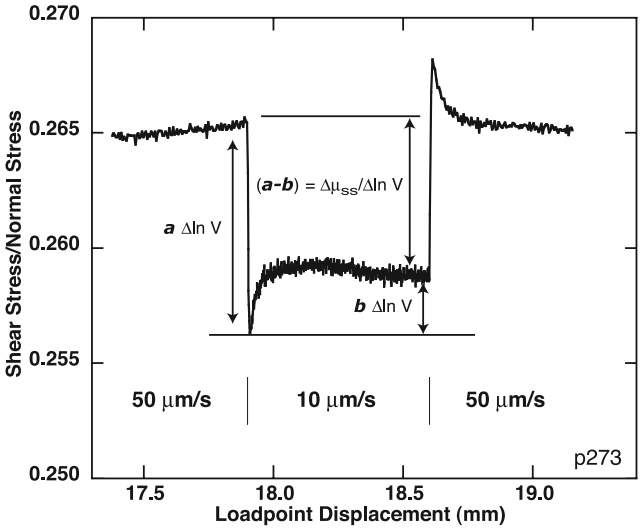

Figure 9. Diagram of a velocity step excerpted from experiment p273. The initial change in friction coefficient scales as $a\ \Delta\ln V$ and is of the same sign. The return to the new steady state coefficient of friction scales as $b\ \Delta\ln V$ and is of the opposite sign. When the velocity dependence $(a-b)$ is positive, the material is said to be velocity strengthening.

Table 2. TOPAS X-Ray Diffraction Results

	Major Phases Present,[a] wt %										Phyllosilicates				
Sample	Quartz	K-Feldspar	Plagioclase	Calcite	Dolomite	Ca-Dolomite	Gypsum	Halite	Hematite	Anatase	Jarosite	Kaolinite	Chlorite	Muscovite	Illite + Smectite	Total Clay
A1	77.7	1.4	1.6	0.2	0.1	0.0	0.0	1.7	0.2	0.3	0.4	0.0	0.6	5.5	9.8	15.9
A2	52.1	1.5	2.1	13.4	13.0	0.0	0.0	0.8	0.3	0.3	0.2	0.2	0.0	1.5	13.7	15.4
A3	17.0	14.3	0.0	0.1	2.0	0.0	0.0	3.0	2.6	0.5	2.9	0.6	0.0	25.7	30.9	57.2
B4	31.3	2.9	4.8	3.5	10.4	2.7	0.6	1.8	0.5	0.4	1.4	1.1	0.0	5.6	32.2	38.9
B5	33.4	7.6	14.8	1.7	0.4	0.0	0.6	1.1	0.1	0.8	1.3	0.5	1.5	1.9	34.3	38.2
B6	9.1	9.7	5.3	8.1	0.4	0.0	1.1	0.1	0.8	1.4	1.0	4.7	20.2	5.8	31.7	62.4
C7	24.0	1.0	3.1	44.0	0.2	0.0	0.2	3.8	0.3	0.2	0.6	1.1	0.0	1.1	19.6	21.8
D8	24.3	2.0	8.8	14.5	0.0	0.0	0.0	0.5	1.7	0.0	0.9	0.8	1.3	10.0	34.7	46.8
E9	62.6	11.4	1.5	0.8	0.0	0.0	3.4	0.4	0.2	0.3	0.1	0.9	0.3	5.0	12.7	18.9
F10	61.5	11.0	6.2	0.2	0.0	0.0	0.5	1.0	0.4	0.3	0.1	0.0	0.7	5.5	11.7	17.9

[a]Phases present in quantities less than 0.5 wt % for all samples are not included.

percentage of expandable (smectitic) interlayers in mixed layer clays, but no additional quantitative measures of nonexpandable versus expandable clays were made.

[19] Interpretation of the diffractograms shows that the dominant crystalline phases are quartz, potassium-feldspar, plagioclase feldspar, and evaporite minerals like halite, and gypsum (Table 2). Samples C7 and D8 contained a substantial calcite phase, probably due to their proximity to carbonate footwall rocks. Total clay content ranged from 15% to 62% by weight in our sample suite (Table 2). We use the term smectite in reference to the undifferentiated clay phases such as montmorillonite, bedillite, and nontronite, which expand when hydrated. Often the term illite is used generically to refer to a group of nonexpandable clay-sized micaceous phases such as muscovite, chlorite, and kaolinite. We reserve illite for the distinct clay phase [*Meunier and Velde*, 2004]. Moreover, illite is typically interlayered with smectite clay phases. Although illite is technically nonexpandable we catalogue it with the expandable smectites since we cannot extract the exact weight percentage of illite.

[20] At sample locations A and B, clay content varied significantly amongst the distinct gouge lithologies present (Table 2). The total clay content of sample A3 was 57 wt % of which, 35 wt % were expandable phases (Table 2). Samples A1 and A2 both have much lower total clay contents of 15.9 wt % and 15.4 wt %, respectively. However, smectites account for the bulk of the clay phases in A1 and A2 with values of 9.8 wt % and 13.7 wt %, respectively. In the field, sample A3 is situated in the core of the gouge zone between A2, which abuts the hanging wall, and A1, which abuts the footwall (Figure 4). A3 has the most pervasive fabric development and appears to include the principle shear zone. Thus our data seem to indicate a correlation between clay content, fabric intensity and the localization of strain in the fault core consistent with observations of a similar low-angle normal fault in Death Valley [*Cowan et al.*, 2003; *Hayman et al.*, 2004].

[21] At location B, total clay content of 62.4% was measured for sample B6; smectites comprise 32 wt % of the sample. Sample B4 and B5 both have a lower total clay content of ~38 wt %. However, smectites comprise over 80 wt % of the total clay phases with values of 32 wt % and 34 wt %, respectively (Table 2). Sample B6 was obtained from the core of the gouge zone, between B5, which abuts the hanging wall, and B4, which abuts the footwall. Sample B6 is the most intensely foliated of these three samples.

[22] Location D is unique in that the gouge layer is highly brecciated but does not have the intense foliation present in all other sample locations. The gouge is relatively clay rich with a total clay content of 46.8 wt % and a smectite content of 34.7 wt % of the sample.

[23] Samples C, E, and F contain less than 30 wt % total clays. Expandable phases, however, make up the majority of clay phases present.

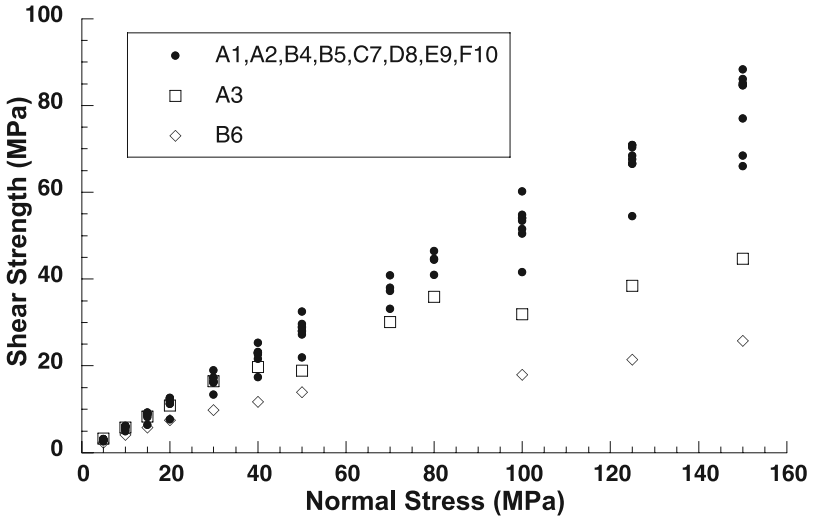

Figure 10. Steady state shear strength (measured at steady state friction) plotted as a function of normal stress. Most samples (circles) plot along a line with slope (μ) = 0.45–0.58, consistent with predicted Byerlee frictional failure. However, both A3 and B6 are significantly weaker. We do not present data for 70 and 80 MPa runs because of technical problems with those runs.

4.2. Friction Experiments

[24] We measured the steady state coefficient of friction, μ_g for all samples at each normal stress by noting the steady state shear strength after 6.5 mm of shear displacement (immediately prior to starting the velocity stepping test) (Figure 8). Most of the samples fit a typical Byerlee friction curve with μ_g ranging from 0.55 to 0.62 (Figure 10). However, two samples (B6 and A3) deviated from the predicted Byerlee values.

[25] We recorded a much broader range of μ_g values for sample B6. At low σ_n, between 5 and 20 MPa μ_g values were ~0.4. At high normal stresses (100–150 MPa), μ_g drops to <0.2. Sample A3 exhibits the most complicated frictional strength response, characterized by significant slip weakening over a range of normal stresses (Figure 11). For sample A3, frictional strength drops substantially between 5 and 50 MPa (Figure 11). We attribute some of the scatter in these data to nonlinearity in the slip weakening behavior.

[26] For sample B6, μ_g decreases linearly with increasing normal stress up to 100 MPa. However, frictional strength remains steady throughout each individual load cycle, with the exceptions for velocity steps and slide-hold-slide sequences (Figure 12a). In contrast, plotting frictional strength against load point displacement for sample A3 shows that frictional strength decreased markedly as load point displacement increased during each load cycle (Figure 12b). Since up to four separate experiments were performed to evaluate frictional strength over the range of applied normal stress, the observed nonlinearity results from the displacement dependence of sample A3. However, the overall decrease in frictional strength for both samples appears to be correlated with the composition of the fault gouge.

[27] Analysis of the friction data in concert with the compositional information from XRD (Table 2) indicates that frictional strength is correlated with the clay content of the fault gouge. The average μ_g of five samples containing <25% clay ranges from 0.55 to 0.63, while the average μ_g of three samples containing between 25% and 50% clay is slightly lower, ranging from 0.48 to 0.59.

[28] Velocity stepping tests allowed us to explore the frictional constitutive behavior of each fault gouge sample

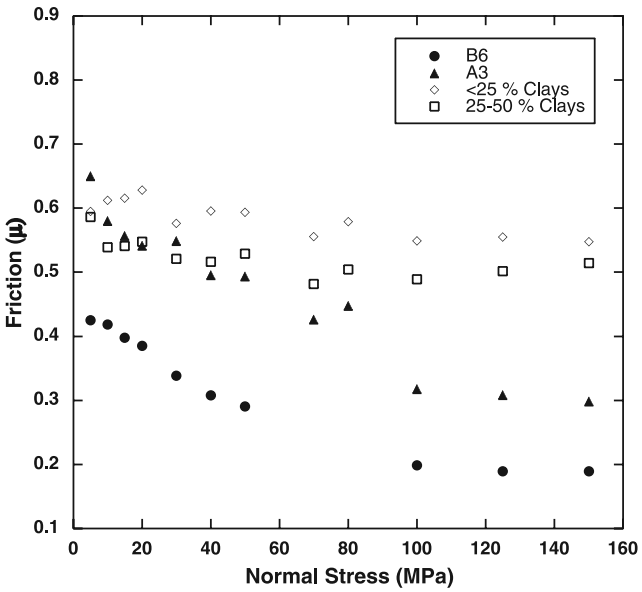

Figure 11. Average coefficient of friction (μ) is plotted as a function of normal stress for samples with <25 wt % total clay phases and 25–50 wt % clay phases. A3 and B6 both contain >50 wt % total clay phases (57% and 62%, respectively); however, we plot them individually rather than averaging them since the frictional response of A3 is complex. We do not present data for 70 and 80 MPa runs due to technical problems with those runs.

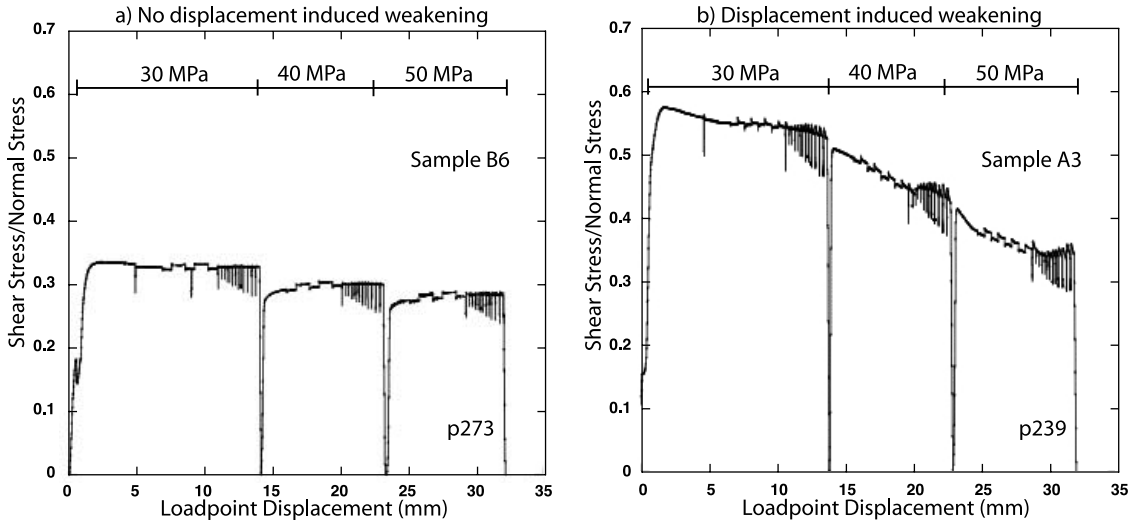

Figure 12. (a) Shear stress/normal stress plotted as a function of displacement for sample B6. This example demonstrates the nearly steady state frictional response we observe for each normal stress step. (b) Shear stress/normal stress plotted as a function of displacement for sample A3. It is clear that strength decreases markedly with increasing displacement. We attribute this to evolution of the fabric within the gouge layer. The ratio of platy minerals to more equant minerals may cause fabric to intensify as displacement increases. Strength appears to reach steady state after 30 mm of displacement, indicative of the establishment of a stable gouge microstructure. For samples exhibiting this behavior, we corrected for displacement-induced weakening.

over the entire range of normal stresses from 5 to 150 MPa. In all cases, we observed velocity strengthening frictional behavior, $(a-b) > 0$, in which frictional strength increased with increasing slip velocity. These data show that $(a-b)$ increases as a function of total clay content (Figure 13a). We observed no such trend in $(a-b)$ as a function of expandable clay content. Previous work by *Saffer and Marone* [2003] showed that typical $(a-b)$ values for illite shale are 0.002–0.004 for up step velocities of 20 μm/s. They did not observe any systematic change in $(a-b)$ as a function of normal stress. Our results are in agreement, as we did not observe changes in $(a-b)$ as a function of normal stress for up step velocities of 40 μm/s; however, we recorded substantially higher values of $(a-b)$ for samples >50% clay (Figure 13b).

5. Discussion

5.1. Relationship Between Friction, Mineralogy, and Clay Content

[29] Our results indicate that the frictional strength of gouge zones in Panamint Valley is dependent on the mineralogy of the fault gouge but not in a simple manner.

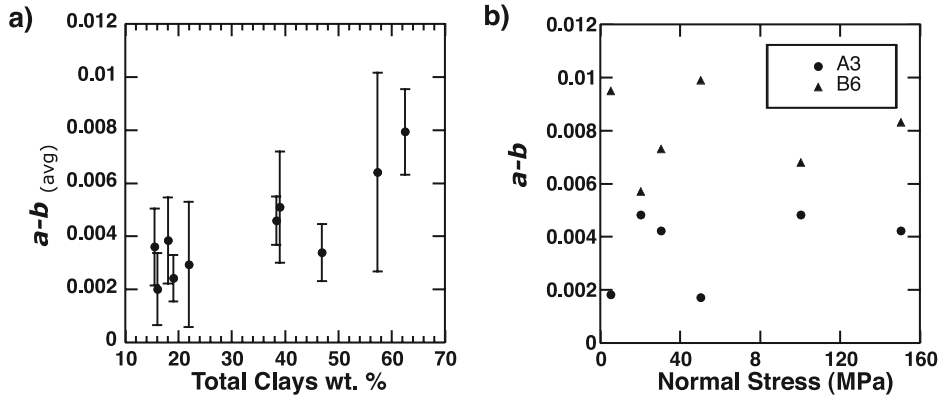

Figure 13. (a) Velocity dependence plotted as a function of clay content. We measured $(a-b)$ at several normal stresses from 5 to 150 MPa for all samples. Averaging $(a-b)$ for each sample suggests the fault gouge becomes more velocity strengthening as clay content increases. Error bars represent 1 std. deviation. (b) Plot of $(a-b)$ versus normal stress for both clay-rich (B6) and clay-poor (A2) samples. These data show that $(a-b)$ does not vary systematically with normal stress.

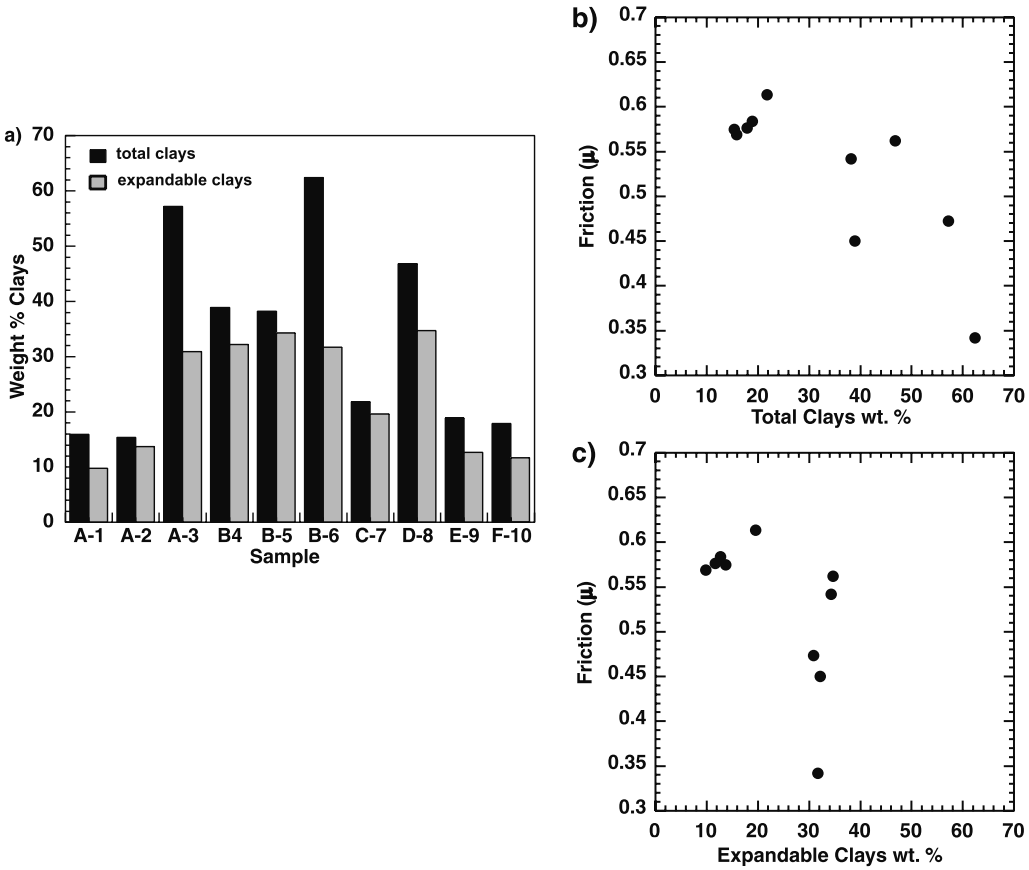

Figure 14. (a) X-ray diffraction results for fault gouge samples. The weight percent of total clay minerals is plotted alongside the weight percent expandable clay minerals for all samples. Samples A3 and B6 are more than 50% clay minerals. (b) Averaged coefficient of friction values from each sample are plotted against the weight percent total clays for each sample. Average coefficient of friction was computed from values at all normal stress steps from 5 MPa to 150 MPa. With increasing clay content, the coefficient of friction decreases. (c) Averaged coefficient of friction values from each are sample plotted against the weight percent expandable clays for each sample. Unlike Figure 14b, no clear relationship exists between frictional strength and abundance of expandable clay minerals.

Friction measurements show that the two samples with more than 50 wt % clay (A3, and B6) are significantly weaker than the other eight samples (Figure 14a). Although there is scatter, we observe a clear decreasing trend in frictional strength as total clay content increases (Figure 14b). Moreover, our results do not suggest any correlation between the presence or abundance of expandable clays and the overall frictional strength of the fault gouge samples (Figure 14c). Given these results we are left to conclude that the overall strength of the fault gouge is more dependent on total clay content than the presence of expandable clay phases. This suggests that caution should be exercised in inferring overall strength of fault gouge from experimental data derived from monomineralic materials.

5.2. Expandable Versus Nonexpandable Clay

[30] Much of the experimental work involving clay gouge has employed monomineralic synthetic gouge analogs [e.g., *Byerlee*, 1978; *Morrow et al.*, 1982; *Logan and Rauenzahn*, 1987; *Morrow et al.*, 2000; *Saffer et al.*, 2001; *Saffer and Marone*, 2003; *Moore and Lockner*, 2004]. Laboratory studies have defined the fundamental frictional properties of the various clay minerals, but they do not address additional complexities germane to natural fault gouge. Natural fault gouge is rarely monomineralic so its strength is not readily compared to the strength of pure clay minerals such as illite or smectite. In addition, pore pressure drainage and grain size distributions may vary widely in natural fault gouge [*Chester et al.*, 2005; *Wilson et al.*, 2005], whereas experiments carried out on synthetic gouge are generally done dry or under drained conditions and often lack a broad grain size/lithology distribution. These synthetic gouge experiments are highly effective in evaluating the strength of fault gouge solely as a function of mineralogy, but the results may not capture potential complexities such as the effect of particle interaction, the presence of interlayered or mixed-phase clays, or undrained conditions associated with poor interparticle fluid drainage, as expected in natural fault gouge.

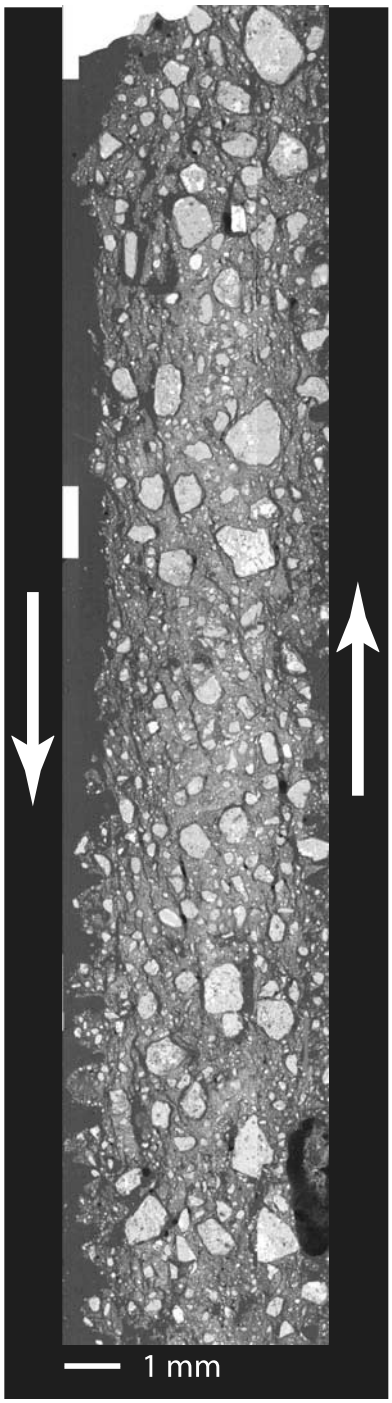

Figure 15. Scanning electron microscope (SEM) image of a layer of A3 fault gouge sheared in the laboratory. Sinistral shear displacement of 15 mm occurred at 5 MPa.

[31] A significant body of work [*Terzaghi and Peck*, 1948; *Lupini et al.*, 1981; *Morrow et al.*, 1982; *Logan and Rauenzahn*, 1987; *Morrow et al.*, 2000; *Saffer et al.*, 2001; *Saffer and Marone*, 2003] has focused on the strength of expandable clay phases (smectites), especially in comparison to the strength of nonexpandable clay phases (e.g., illite). Illite has a coefficient of friction of ~0.6 [*Saffer and Marone*, 2003], similar to most lithologies [*Byerlee*, 1978]. Smectites have been shown to have a much lower coefficient of friction of 0.1–0.3, depending on hydration state [*Byerlee*, 1978; *Morrow et al.*, 1982; *Saffer and Marone*, 2003]. Differences in the frictional properties and stability has been investigated as a potential driver of seismogenesis in subduction zones [*Vrolijk and van der Pluijm*, 1999; *Saffer et al.*, 2001; *Brown et al.*, 2003]. Although the contrast in strength between these end-members is clear in laboratory studies, it is difficult to predict the influence individual clay phases have on the overall strength of natural fault gouge. Pure smectite and illite end-members are virtually nonexistent in natural gouge. The clay phases often classified as smectites by XRD analysis are typically mixed–layer clays composed of both expandable layers as well as nonexpandable layers, more accurately described as a smectite-illite continuum [*Meunier and Velde*, 2004].

[32] Our findings indicate that the production of weak fault gouge is not dependent on the presence of intrinsically weak clay phases such as smectite, but that the weakening mechanism/s must depend on some property common to all clay phases.

5.3. Fault Weakening Mechanisms

[33] If the frictional strength of the fault gouge is dependent only on the total clay content, it begs the question of how the abundance of clay minerals effectively weakens the gouge layer. Our observations of displacement-induced weakening in sample A3 (Figure 12b) provide some insight into this question. Although both A3 and B6 exhibit weakening with increases in normal stress (Figure 11) the mechanisms are unique.

[34] The strength of A3 decreases as displacement increases during each normal stress step. Sample A3 is composed of a heterogeneous mix of clay phases and durable quartz grains; thus strong slip weakening in this case may be due to gradual shear localization and foliation development (Figure 15) [*Bos and Spiers*, 2001, 2002]. If the intensity of the foliation increased gradually, the initial load history we imposed may have established only a weak foliation that continued to intensify as displacement increased, causing continued weakening.

[35] The particle size distribution of sample B6 is much more homogenous, nearly all of the grains are clay-sized. Thus we posit that shear localization and foliation developed rapidly, resulting in a steady state frictionally weak gouge zone. The frictional strength of B6 decreases in a step function manner with increasing normal stress (Figure 12a). Each increase in normal stress induces compaction and enhances the existing shear fabric, resulting in decreased frictional strength.

[36] From the outcome of our experiments, it seems that both the alignment and the orientation of flat platy layers around larger more equant quartz or feldspar grains decrease the overall strength of the fault gouge as displacement continues [e.g., *Collettini and Holdsworth*, 2004]. *Mair et al.* [2002] and *Anthony and Marone* [2005] demonstrated the effect of grain angularity on frictional strength and

stability of synthetic fault gouge. Gouge composed of angular grains is stronger and more stable due to increased particle interlocking and reduced rolling efficiency [*Morgan*, 1999; *Morgan and Boettcher*, 1999; *Mueth et al.*, 2000; *Mair et al.*, 2002]. Our data suggest that an abundance of aligned clay minerals in the matrix may act as a lubricant between grain-grain contacts, minimizing interlocking and dilation, while localizing strain within the clay-rich matrix. This is consistent with the numerical results of *Morgan and Boettcher* [1999], which show that an abundance of fine-grained particles produce localized shear zones and reduced interparticle friction. In coarse-grained samples without a fine-grained matrix, the frictional coupling between the grains (e.g., interlocking) caused widely distributed deformation and abundant interparticle rolling [*Morgan and Boettcher*, 1999]. In our model, weakening is dependent primarily on the development of shear planes, since both expandable as well as nonexpandable clays share the same platy habit, they are equally effective in localizing strain onto discrete shear planes.

5.4. Implications for Weak Low-Angle Normal Faults

[37] Our experiments provide insight into the behavior of fault gouge in Panamint Valley and similar extensional settings. The results of these laboratory experiments demonstrate that the strength of natural fault gouge may be much lower than the frequently assumed value of $\mu_g = 0.6$. These results are important because they enhance our understanding of the mechanics governing low-angle normal faulting and imply that active slip is possible even for shallowly dipping fault planes (LANFS), regardless of any additional weakening due to abnormal fault zone fluid pressure, though we recognize that elevated fluid pressures would weaken the fault further. We sampled fault gouge in situ and subjected the gouge to minimal processing, therefore we can be confident that the results are conservative estimates of the maximum strength (given the high laboratory strain rate) of fault rocks in Panamint Valley, and that they represent an improvement upon estimates made using synthetic substitutes. Our results reinforce the intuitive understanding that natural fault gouge zones are inherently heterogeneous. For example, three samples from location A exhibit dramatic differences in behavior, yet all three were collected within a meter of the fault core. Sample A3 was sampled from the intensely foliated core, and is much weaker than samples A1 and A2, which were extracted from the top and bottom edges of the gouge zone. This degree of variability hints that we should expect to observe significant along-strike and downdip changes in gouge strength. Pressure, temperature, lithology, and fluid content all influence the composition of fault zone rocks. Our results suggest that the fabric imparted upon fault gouge may be an important factor in determining frictional strength.

[38] It is important to ask how fabric and microstructures evolve with time, displacement, and the changing environmental factors mentioned above. On the basis of the focus of much of the literature pertaining to the strength of fault gouge [*Byerlee*, 1978; *Logan and Rauenzahn*, 1987; *Saffer et al.*, 2001; *Saffer and Marone*, 2003; *Moore and Lockner*, 2004; *Anthony and Marone*, 2005], it is easy to conclude that frictional properties of fault gouge are determined at the grain scale, but mesoscale fabrics may also affect the overall strength of the fault [*Chester and Logan*, 1986, 1987; *Logan et al.*, 1992].

[39] To this end, a germane question to the mechanics of low-angle normal faulting in Panamint Valley is the depth at which the weak fault gouge observed at the surface was generated. We can provide broad constraints on the depth of gouge generation using rates of abrasive frictional wear [*Scholz*, 1987] and fault gouge mineralogy [*Pytte and Reynolds*, 1988]. *Scholz* [1987] showed that fault gouge thickness scales linearly with total fault slip for a given normal stress and rock type. This ratio (wear rate) is typically between 10^{-3} and 10^{-1} and increases with increasing normal stress. Because of the normal stress dependency, it is unlikely that the 0.5–1.5 m thick gouge zones in Panamint Valley formed in situ. In the shallow part of the fault, at low normal stress, the wear rate is effectively zero and fault gouge is not produced [*Yoshioka*, 1986]. The observation that the gouge zone does not incorporate material from the moderately consolidated hanging wall further corroborates the hypothesis that the observed gouge zone was produced at depth and has been translated to its present-day elevation through exhumation of the footwall.

[40] To evaluate this hypothesis, we use laboratory results of *Yoshioka* [1986] showing that wear rate is negligible below $\sigma \sim 15$–20 MPa. This corresponds to a depth of $\sim$1 km in Panamint Valley (using an effective lithostatic stress gradient of $\sigma_{eff} \sim 17$ MPa/km), which would indicate that the fault wear rate becomes zero for depths shallower than this threshold. If we assume a steady state wear rate of 10^{-2} [*Scholz*, 1987] for conditions where $\sigma_{eff} > 17$ MPa, and no decrease in gouge zone thickness as it is exhumed, the generation of the observed $\sim$1 m thick gouge zone requires $\sim$100 m of fault offset. This implies that the depth of gouge formation is within the range of 1–1.5 km below the surface. Total fault offset required to exhume the accumulated fault gouge from this depth is $\sim$3–4 km given the 20° dip of the low-angle normal fault (Figure 3b). Assuming some degree of chemical alteration during gouge formation would decrease the required displacement further. Leveraging typical wear rates in the estimate above constrains the minimum depth of gouge formation. To constrain the maximum depth of gouge formation, we can use results of the XRD analyses, which show that most samples contain >20 wt % expandable (smectitic) clay phases. Since smectite transforms to illite above T = 150°C the fault gouge in Panamint Valley could not have been generated below a depth of 4–5 km given the thermal structure of the lithosphere in the Basin and Range [*Lachenbruch and Sass*, 1977]. Using an average Pleistocene-present slip rate of 2.5 mm/yr [*Zhang et al.*, 1990], the age of the fault gouge could be roughly estimated at $\sim$1.2–1.6 Ma. This estimate would be much improved through the application of in situ dating techniques such as $^{40}Ar/^{39}Ar$ [*van der Pluijm et al.*, 2001].

[41] Although the above bounds are admittedly quite coarse, the observations above suggest that the weak fault rocks we documented in outcrop at the surface may mantle

the fault contact to depths of 1 to 5 km. The possibility of a pervasive zone of weak fault rocks that extends below 1 km would imply that active slip is likely aseismic in shallow basins floored by detachment faults like Panamint Valley [*Burchfiel et al.*, 1987; *MIT 1985 Field Geophysics Course and Biehler*, 1987] and perhaps others in the Basin and Range [*Cichanski*, 2000].

6. Conclusions

[42] Our results provide constraint on the frictional properties of fault gouge from a documented low-angle normal fault in Panamint Valley. In addition, our data highlight the inadequacies in the way the mechanical properties of fault zones are generically characterized. Although investigations commonly assume a steady state coefficient of friction of 0.6 for fault rocks, we have demonstrated that certain fault gouges from Panamint Valley have a coefficient of friction less than 0.2.

[43] XRD analyses of gouge samples reveal the spatial heterogeneity of fault gouge composition. Our results show that frictional strength decreases with increasing clay content. Clay-rich fault gouge likely mantles other LANF structures similar to the Panamint Valley fault system studied here, so it is reasonable that these gouge zones are anomalously weak as well. If it is plausible to assume the overall strength of the fault is controlled by the strength of the fault gouge, the low coefficient of friction allows planes dipping less than 30° to fail via frictional sliding (Figure 1). We conclude that slip on low-angle fault segments in Panamint Valley is facilitated in large part by the presence of anomalously weak fault gouge.

[44] **Acknowledgments.** Reviews by C. Collettini, B. van der Pluijm, and an anonymous reviewer greatly improved the manuscript. This work has been funded by National Science Foundation grants EAR 0196570, OCE 0196462, and EAR-0337627 to C.J.M., EAR 0409169 to E.K., Sigma Xi, Geological Society of America, American Association of Petroleum Geologists, and P.D. Krynine Memorial fund grants to T.J.N.

References

Abers, G. A., C. Z. Mutter, and J. Fang (1997), Shallow dips of normal faults during rapid extension: Earthquakes in the Woodlark-D'Entrecasteaux rift system, Papua New Guinea, *J. Geophys. Res.*, *102*, 15,301–15,317.

Anderson, E. M. (1951), *The Dynamics of Faulting*, 206 pp., Olivier and Boyd, White Plains, N. Y.

Andrew, J. E., and J. D. Walker (2003), Miocene and Pliocene volcanic-sedimentary successions and relationships with deformation in the extensionally dismembered Panamint Valley region, SE California, *Geol. Soc. Am. Abstr. Programs*, *35*, 347.

Anthony, J. L., and C. Marone (2005), Influence of particle characteristics on granular friction, *J. Geophys. Res.*, *110*, B08409, doi:10.1029/2004JB003399.

Axen, G. J. (1992), Pore pressure, stress increase, and fault weakening in low-angle normal faulting, *J. Geophys. Res.*, *97*, 8979–8991.

Axen, G. J. (1999), Range-front fault scarps of the Sierra El Mayor, Baja California: Formed above an active low-angle normal fault?, *Geology*, *27*, 247–250.

Axen, G. J. (2004), Mechanics of low-angle normal faults, in *Rheology and Deformation of the Lithosphere at Continental Margins*, edited by G. D. Karner, B. Taylor, N. W. Driscoll, and D. L. Kohlstedt, pp. 46–91, Columbia Univ. Press, New York.

Bos, B., and C. J. Spiers (2001), Experimental investigation into the microstructural and mechanical evolution of phyllosilicate-bearing fault rock under conditions favouring pressure solution, *J. Struct. Geol.*, *23*, 1187–1202.

Bos, B., and C. J. Spiers (2002), Frictional-viscous flow of phyllosilicate-bearing fault rock: Microphysical model and implications for crustal strength profiles, *J. Geophys. Res.*, *107*(B2), 2028, doi:10.1029/2001JB000301.

Brown, K. M., A. Kopf, M. B. Underwood, and J. L. Weinberger (2003), Compositional and fluid pressure controls on the state of stress on the Nankai subduction thrust: A weak plate boundary, *Earth Planet. Sci. Lett.*, *214*, 589–603.

Burchfiel, B. C., and J. H. Stewart (1966), 'Pull-apart' origin of the central segment of Death Valley, California, *Geol. Soc. Am. Bull.*, *77*, 439–441.

Burchfiel, B. C., K. V. Hodges, and L. H. Royden (1987), Geology of Panamint Valley–Saline Valley pull-apart system, California: Palinspastic evidence for low-angle geometry of a Neogene range-bounding fault, *J. Geophys. Res.*, *92*, 10,422–10,426.

Byerlee, J. D. (1978), Friction of rocks, *Pure Appl. Geophys.*, *116*, 615–626.

Caskey, S. J., S. G. Wesnousky, P. Zhang, and D. B. Slemmons (1996), Surface faulting of the 1954 Fairview Peak (M_S 7.2) and Dixie Valley (M_S 6.8) earthquakes, central Nevada, *Bull. Seismol. Soc. Am.*, *86*, 761–787.

Chester, F. M., and J. M. Logan (1986), Implications for the mechanical properties of brittle faults from observations of the Punchbowl fault zone, California, *Pure Appl. Geophys.*, *124*, 79–106.

Chester, F. M., and J. M. Logan (1987), Composite planar fabric of gouge from the Punchbowl fault, California, *J. Struct. Geol.*, *9*, 621–634.

Chester, J. S., F. M. Chester, and A. K. Kronenberg (2005), Fracture surface energy of the Punchbowl fault, San Andreas system, *Nature*, *437*, 133–136.

Cichanski, M. (2000), Low-angle, range-flank faults in the Panamint, Inyo, and Slate ranges, California: Implications for recent tectonics of the Death Valley region, *Geol. Soc. Am. Bull.*, *112*, 871–883.

Collettini, C., and R. E. Holdsworth (2004), Fault zone weakening processes along low-angle normal faults: Insights from the Zuccale fault, Isle of Elba, Italy, *J. Geol. Soc.*, *161*, 1039–1051.

Collettini, C., N. De Paola, R. E. Holdsworth, and M. R. Barchi (2006), The development and behaviour of low-angle normal faults during Cenozoic asymmetric extension in the northern Appenines, Italy, *J. Struct. Geol.*, *28*, 333–352.

Cowan, D. S., T. T. Cladouhos, and J. K. Morgan (2003), Structural geology and kinematic history of rocks formed along low-angle normal faults, Death Valley, California, *Geol. Soc. Am. Bull.*, *115*, 1230–1248.

Floyd, J. S., J. C. Mutter, A. M. Goodliffe, and B. Taylor (2001), Evidence for fault weakness and fluid flow within an active low-angle normal fault, *Nature*, *411*, 779–783.

Handin, J. (1969), On the Coulomb-Mohr failure criterion, *J. Geophys. Res.*, *74*, 5343–5348.

Hayman, N. W., J. R. Knott, D. S. Cowan, E. Nemser, and A. M. Sarna-Wojcicki (2003), Quaternary low-angle slip on detachment faults in Death Valley, California, *Geology*, *31*, 343–346.

Hayman, N. W., B. A. Housen, T. T. Cladouhos, and K. Livi (2004), Magnetic and clast fabrics as measurements of grain-scale processes within the Death Valley shallow crustal detachment faults, *J. Geophys. Res.*, *109*, B05409, doi:10.1029/2003JB002902.

Hodges, K. V., L. W. McKenna, and M. B. Harding (1990), Structural unroofing of the central Panamint Mountains, Death Valley region, southeastern California, in *Basin and Range Extensional Tectonics Near the latitude of Las Vegas, Nevada*, edited by B. Wernicke, *Mem. Geol. Soc. Am.*, *176*, 377–390.

Jackson, J. A., and N. J. White (1989), Normal faulting in the upper continental crust: Observations from regions of active extension, *J. Struct. Geo.*, *11*, 15–36.

Kirby, E., N. Snyder, K. Whipple, J. D. Walker, and J. Andrew (2003), Neotectonics of the Panamint Valley fault zone: Active slip on a low-angle normal fault system, *Eos Trans. AGU*, *84*(46), Fall Meet. Suppl., Abstract T51D-0194.

Lachenbruch, A. H., and J. H. Sass (1977), Models of an extending lithosphere and heat flow in the basin and Range province, in *Cenozoic Tectonics and Regional Geophysics of the Western Cordillera*, edited by R. B. Smith and G. P. Eaton, *Mem. Geol. Soc. Am.*, *152*, 209–250.

Logan, J. M., and K. A. Rauenzahn (1987), Frictional dependence of gouge mixtures of quartz and montmorillnite on velocity, composition, and fabric, *Tectonophysics*, *144*, 87–108.

Logan, J. M., C. A. Dengo, N. G. Higgs, and Z. Z. Wang (1992), Fabrics of experimental fault zones: Their development and relationship to mechanical behavior, in *Fault Mechanics and Transport Properties of Rocks*, edited by B. Evans and T. F. Wong, pp. 33–67, Elsevier, New York.

Longwell, C. R. (1945), Low-angle normal faults in the Basin and Range Province, *Eos AGU Trans.*, *26*, 107–118.

Lupini, J. F., J. F. Skinner, and A. E. Vaughan (1981), The drained residual strength of cohesive soils, *Geotechnique*, *31*, 181–213.

Mair, K., K. M. Frye, and C. Marone (2002), Influence of grain characteristics on the friction of granular shear zones, *J. Geophys. Res.*, *107*(B10), 2219, doi:10.1029/2001JB000516.

Marone, C. (1998), Laboratory-derived friction laws and their application to seismic faulting, *Annu. Rev. Earth Planet. Sci.*, *26*, 643–696.

Meunier, A., and B. Velde (2004), *Illite*, Springer, New York.

MIT 1985 Field Geophysics Course, and S. Biehler (1987), A geophysical investigation of the northern Panamint Valley, Inyo County, California: Evidence for possible low-angle normal faulting at shallow depth in the crust, *J. Geophys. Res.*, *92*, 10,427–10,441.

Molnar, P., and W. P. Chen (1982), Seismicity and mountain building, in *Mountain Building Processes*, edited by K. J. Hsu, pp. 41–57, Elsevier, New York.

Moore, D. E., and D. A. Lockner (2004), Crystallographic controls on the frictional behavior of dry and water-saturated sheet structure minerals, *J. Geophys. Res.*, *109*, B03401, doi:10.1029/2003JB002582.

Moore, D. M., and R. C. J. Reynolds (1997), *X-Ray Diffraction and the Identification and Analysis of Clay Minerals*, Oxford Univ. Press, New York.

Morgan, J. K. (1999), Numerical simulations of granular shear zones using the distinct element method: 2. Effects of particle size distribution and interparticle friction on mechanical behavior, *J. Geophys. Res.*, *104*, 2721–2732.

Morgan, J. K., and M. S. Boettcher (1999), Numerical simulations of granular shear zones using the distinct element method: 1. Shear zone kinematics and the micromechanics of localization, *J. Geophys. Res.*, *104*, 2703–2719.

Morrow, C. A., L. Q. Shi, and J. D. Byerlee (1982), Strain hardening and strength of clay-rich fault gouges, *J. Geophys. Res.*, *87*, 6771–6780.

Morrow, C. A., D. E. Moore, and D. A. Lockner (2000), The effect of mineral bond strength and absorbed water on fault gouge frictional strength, *Geophys. Res. Lett.*, *27*, 815–818.

Mueth, D. M., G. F. Debregeas, G. S. Karczmar, P. J. Eng, S. R. Nagel, and H. M. Jaeger (2000), Signatures of granular microstructure in dense shear flows, *Nature*, *406*, 385–388.

Piccinini, D., et al. (2003), Microseismic study in a low seismicity area of Italy: The Citta di Castello 2000–2001 experiment, *Ann. Geophys.*, *46*, 1315–1324.

Pytte, A. M., and R. C. J. Reynolds (1988), The thermal transformation of smectite to illite, in *Thermal Histories of Sedimentary Basins*, edited by T. H. McCulloh and N. D. Naeser, pp. 133–140, Springer, New York.

Rice, J. R. (1992), Fault stress states, pore pressure distributions, and the weakness of the San Andreas fault, in *Fault Mechanics and Transport Properties in Rocks*, edited by B. Evans and T. F. Wong, pp. 475–503, Elsevier, New York.

Rietveld, H. M. (1969), A profile refinement method for nuclear and magnetic structures, *J. Appl. Crystallogr.*, *2*, 65–71.

Ruina, A. L. (1983), Slip instability and state variable friction laws, *J. Geophys. Res.*, *88*, 10,359–10,370.

Saffer, D. M., and C. J. Marone (2003), Comparison of smectite- and illite-rich gouge frictional properties: Application to the updip limit of the seismogenic zone along subduction megathrusts, *Earth Planet. Sci. Lett.*, *215*, 219–235.

Saffer, D. M., K. M. Frye, C. J. Marone, and K. Mair (2001), Laboratory results indicating complex and potentially unstable frictional behavior of smectite clay, *Geophys. Res. Lett.*, *28*, 2297–2300.

Scholz, C. H. (1987), Wear and gouge formation in brittle faulting, *Geology*, *15*, 493–495.

Scholz, C. H. (2002), *The Mechanics of Earthquakes and Faulting*, 471 pp., Cambridge Univ. Press, New York.

Smith, R. S. U. (1973), Tectonic deformation of pluvial-lake terraces along the Panamint Valley fault zone, eastern California, *Geol. Soc. Am. Abstr. Programs*, *5*, 108–109.

Snyder, N. P., and K. V. Hodges (2000), Depositional and tectonic evolution of a supradetachment basin: $^{40}Ar/^{39}Ar$ geochronology of the Nova Formation, Panamint Range, California, *Basin Res.*, *12*, 19–30.

Terzaghi, K., and R. B. Peck (1948), *Soil Mechanics in Engineering Practice*, 566 pp., John Wiley, Hoboken, N. J.

Thatcher, W., and D. P. Hill (1991), Fault orientations in extensional and conjugate strike-slip environments and their implications, *Geology*, *19*, 1116–1120.

van der Pluijm, B. A., C. A. Hall, P. Vrolijk, D. R. Pevear, and M. Covey (2001), The dating of shallow faults in the Earth's crust, *Nature*, *412*, 172–174.

Vrolijk, P., and B. A. van der Pluijm (1999), Clay gouge, *J. Struct. Geol.*, *21*, 1039–1048.

Wernicke, B. (1995), Low-angle normal faults and seismicity: A review, *J. Geophys. Res.*, *100*, 20,159–20,174.

Wernicke, B. P., and G. J. Axen (1988), On the role of isostacy in the evolution of normal fault systems, *Geology*, *16*, 848–851.

Westaway, R. (1999), The mechanical feasibility of low-angle normal faulting, *Tectonophysics*, *308*, 407–443.

Wilson, B., T. Dewers, Z. Reches, and J. Brune (2005), Particle size and energetics of gouge from earthquake rupture zones, *Nature*, *434*, 749–752.

Yin, A. (1989), Origin of regional rooted low-angle normal faults: A mechanical model and its tectonic implications, *Tectonics*, *8*, 469–482.

Yoshioka, N. (1986), Fracture energy and the variation of gouge and surface roughness during frictional sliding of rocks, *J. Phys. Earth*, *34*, 335–355.

Zhang, P., M. Ellis, D. B. Slemmons, and F. Mao (1990), Right-lateral displacements and the Holocene slip rate associated with prehistoric earthquakes along the southern Panamint Valley fault zone: Implications for southern Basin and Range tectonics and coastal California deformation, *J. Geophys. Res.*, *95*, 4857–4872.

E. Kirby and C. Marone, Department of Geosciences, Pennsylvania State University, 336 Deike Bldg., University Park, PA 16802-0000, USA.

T. Numelin, ExxonMobil Exploration Company, 233 Benmar Drive, Houston, TX 77060, USA. (tye.j.numelin@exxonmobil.com)